Check for updates

ADVANCED MATERIALS
www.advmat.de

Ultrasensitive Touch Sensor for Simultaneous Tactile and Slip Sensing

Yue Liu, Juan Tao, Yepei Mo, Rongrong Bao, and Caofeng Pan**

Touch is a general term to describe mechanical stimuli. It is extremely difficult to develop touch sensors that can detect different modes of contact forces due to their low sensitivity and data decoupling. Simultaneously conducting tactile and slip sensing presents significant challenges for the design, structure, and performance of sensors. In this work, a highly sensitive sandwich-structured sensor is achieved by exploiting the porosity and compressive modulus of the sensor's functional layer materials. The sensor shows an ultra-high sensitivity of 1167 kPa^{-1} and a low-pressure detection limit of 1.34 Pa due to its considerably low compression modulus of 23.8 Pa. Due to this ultra-high sensitivity, coupled with spectral analysis, it allows for dual-mode detection of both tactile and slip sensations simultaneously. This novel fabrication strategy and signal analysis method provides a new direction for the development of tactile/slip sensors.

1. Introduction

Intelligent touch sensors are used in various fields to control a target object, e.g., these sensors provide robots with human-like grasping capabilities.[1] A human tactile nerve perceives the world through the pressure generated when its surface is deformed during contact with an object.[2] Similar to human skin, an ideal touch sensor should accurately recognize various contact forces, such as normal pressure, slipping, and shear force.[3] Most research on touch sensors has focused on tactile sensing, and significant breakthroughs have been achieved in complementary sensing principles, material modification, and construction of device structures.[4]

As shown in **Figure 1a**, when a human hand can detect only tactile sensations but not slipping, it is difficult to determine the relative motion state of a sensor and the contact object.[5] Furthermore, material information, such as the object's surface roughness, cannot be determined. There has been negligible research on touch sensors suitable for tactile/slip sensing. Most advanced slip sensors are based on an array device design.[6] The slip sensing strategy implemented in multipixel design depends on large changes in the location of the detected target.[7] There have been only a few studies on individual touch sensors with tactile/slip modes. A flexible tactile sensor based on hierarchical microstructures and nanostructures has been reported to discriminate between normal and shear forces using significant differences in response times.[8] In addition, the stick-slip phenomenon that occurs during slip motion has been used to develop a multifunctional bionic tactile system based on a stick-slip sensing strategy. This system demonstrates high recognition rates in slippage detection.[9] Although these studies have presented new ideas for the development of tactile/slip sensors, the different pressure sensations generated by fixed normal pressure and slip pressure have not been examined during contact between a human hand and the rough surface of an object (Figure 1b).

In general, it is not simple for the human body to feel slip. First, it is necessary to detect the sensation of touch through the skin. This is similar to signal acquisition by a sensor, requiring low-level processing (Figure 1c). In addition, advanced analysis by the brain is required to achieve perception (Figure 1d), which involves information integration and feature extraction.[10] Therefore, it has been speculated that the sensitivity of pressure sensors is limited because of conventional fabrication techniques. This makes it difficult to obtain details about signals and ensure accuracy in distinguishing between different contact states.

The microstructures of sensors play a key role in improving sensitivity. Compressibility and normalized change in the contact area are two important factors that affect the sensing properties of touch sensors.[11] A porous polymer can serve as a 3D skeleton to effectively regulate the structural stiffness and compressibility of materials by changing structural parameters such as the porosity and elastic modulus. Conventional strategies, such as the use of commercial sponges or foams, freeze-drying techniques, and sacrificial template techniques, typically require expensive equipment and long experimental durations.[12] The formation of films using phase inversion with the sacrificial template method is an innovative mass-transfer process that involves a change in the phase state of a material. A controllable interconnected porous film can be formed only through a material system composed of a

Y. Liu, J. Tao, Y. Mo, R. Bao, C. Pan
Beijing Institute of Nanoenergy and Nanosystems
Chinese Academy of Sciences
Beijing 101400, China
E-mail: baorongrong@binn.cas.cn; pancaofeng@buaa.edu.cn
R. Bao, C. Pan
Institute of Atomic Manufacturing
Beihang University
Beijing 100191, P. R. China

The ORCID identification number(s) for the author(s) of this article can be found under https://doi.org/10.1002/adma.202313857

DOI: 10.1002/adma.202313857

 © 2024 Wiley-VCH GmbH

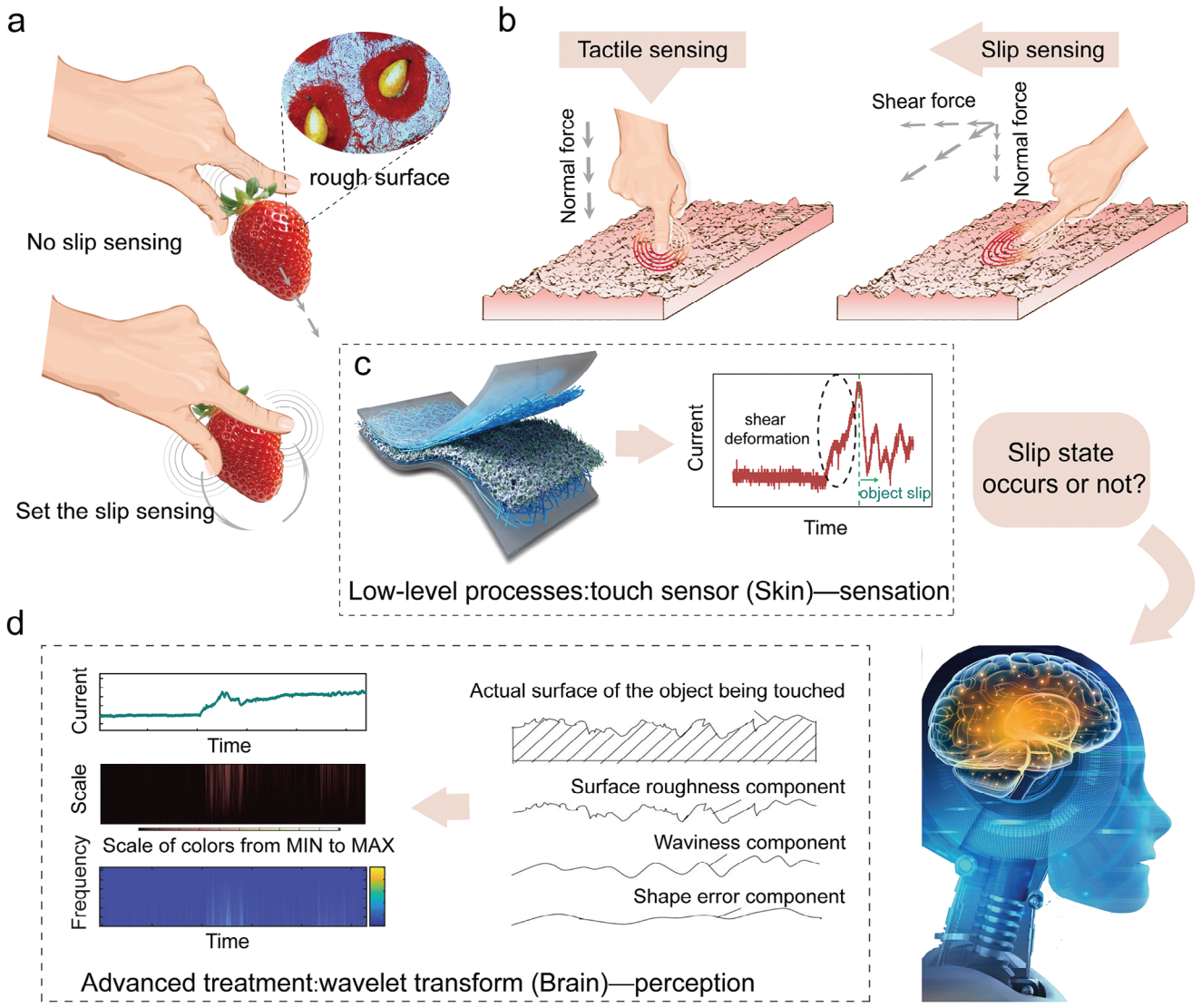

Figure 1. Significance of slip sensing and its realization strategy. a) Schematic diagram of the difference between the presence and absence of slip sensing for grasping object states. The inset shows an optical microscopy image of the rough surface of a strawberry. b) Two modes of pressure-sensitive haptics: tactile sensing and slip sensing. Tactile sensing involves finger-fixed contact with the rough surface of an object, which can sense only pressure and cannot identify the pressure perception gap. Slip sensing can be used to determine the state of an object by moving the finger over the rough surface of the object, feeling the curvature and the presence of edges through protrusions and changes in pressure. c) Low-level processes. Different sensing signals for tactile and slip sensing of objects are captured using ultrasensitive touch sensors. d) Advanced treatment. Features are integrated and extracted from the collected signals to achieve machine perception.

polymer, solvent, and nonsolvent.[13] The process of this method is simple and efficient, does not need to rely on bulky large-scale equipment, only basic experimental instruments are required, the sensor-sensitive layer preparation process requires only one-step molding, the processing time is about 10 s, and the controllability and universality of the prepared membranes can be better adjusted according to the membrane's desired application of the structure and performance of the membrane.

Ultrahigh sensitivity is needed to achieve complex tactile perception, such as the simultaneous detection of positive pressure and slip states. In this study, we developed an ultrasensitive piezoresistive touch sensor using a one-step phase-inversion-to-film strategy with the sacrificial template (PI-ST) method. Additionally, we performed spectral analysis of the output signal using wavelet transform to enable sensor application for pressure and slip detection. The touch sensor achieved an ultrahigh sensitivity of 1167 kPa^{-1} at pressures below 1179 Pa and a sensitivity of 25 kPa^{-1} at pressures of 1179–10 240 Pa due to its extremely low compression modulus of 23.8 Pa and good compressibility of the active layer with an interconnected porous structure. The minimum detectable pressure of the sensor was ≈1.34 Pa, and the sensor could be stably operated for more than 2000 loading–unloading cycles under a load of 500 Pa. Additionally, the detection of extremely low static pressure, dynamic pressure, weak physiological signals, and weak vibrations was demonstrated to verify the robust performance of the touch sensor in practical

© 2024 Wiley-VCH GmbH

15214095, 0, Downloaded from https://onlinelibrary.wiley.com/doi/10.1002/adma.202313857 by Cas-Beijing Institution Of, Wiley Online Library on [19/03/2024]. See the Terms and Conditions (https://onlinelibrary.wiley.com/terms-and-conditions) on Wiley Online Library for rules of use; OA articles are governed by the applicable Creative Commons License

applications. The output signal was processed using a wavelet transform to obtain the frequency-domain characteristics of the slip signal, allowing slip to be detected and various materials to be identified. The recognition accuracy of tactile and slip signals was improved using machine learning algorithms. In this paper, we show that, compared with the current class of touch sensors, our proposed touch sensor achieves the best sensing sensitivity, detection range, and detection limits. Currently, only aerosol-based sensors have similar sensitivity, albeit with a much narrower detection range.[14] Therefore, our sensors can robustly detect complex contact states, including pressure and slip. The fabrication strategy for the ultrasensitive tactile sensor and the combination of the sensor with data characterization tools can provide a new pathway for the construction of individual tactile/slip sensors with high potential for the development of intelligent manipulators.

2. Results and Discussion

2.1. Design Concept and Principle of a Touch Sensor Based on the PI-ST Method

The steps for designing a sensitive layer with an interconnected porous structure are shown in **Figure 2a**. The ternary material system used in the PI-ST method consists of a polymer, solvent, and nonsolvent, i.e., thermoplastic polyurethane (TPU)/Ag nanowire (NW)/NaCl composite materials, *N*,*N*-dimethylformamide (DMF), and a Ag NW aqueous (Ag NW aq.) solution, respectively. The interconnected porous structure of the conductive TPU film is constructed during the PI-ST process by introducing Ag NWs as conductive fillers and soluble NaCl particles as sacrificial templates.

The one-step formation mechanism of the conductive TPU film is analyzed based on thermodynamics and kinetics. In terms of thermodynamics, a ternary phase diagram of this material system is drawn on the basis of Flory–Huggins theory (Figure 2b). P, S, and NS represent the polymer (TPU/Ag NW/NaCl composite materials), solvent (DMF), and nonsolvent (Ag NW aq. solution), respectively. A represents the composition of the initial casting liquid (DMF solution of TPU/Ag NW/NaCl). The casting liquid enters the phase separation zone under the action of DMF and the Ag NW aq. solution, thus forming two equilibrium liquid phases (B' and B'') to realize phase inversion. The expressions for the free energy and interaction parameters of this ternary material system are provided (Equation (S1) and Table S1, Supporting Information).[15a] From the perspective of kinetics, when TPU is initially immersed in the Ag NW aq. solution, overall movement and migration cannot occur because of its large molecular weight. However, the Ag NW aq. solution shows a low diffusion resistance to DMF. Therefore, the mass of DMF that is removed from the polymer solution is greater than the mass of the Ag NW aq. solution that is added to the polymer solution. This results in a rapid increase in the TPU concentration, and the components of the polymer solution are rapidly separated through the metastable zone. The expression for the apparent diffusion coefficient is shown in Equation (S2) in the Supporting Information.[15b]

Different pores are formed during phase inversion. However, the surface solvent continuously evaporates into the interior and pores of aggregates, resulting in smaller pores. Although this process can be controlled to modulate the micropore morphology, it is still difficult to obtain an interconnected porous structure when only phase inversion is used.[16] Therefore, NaCl particles are used as sacrificial templates to resolve this issue. The scanning electron microscope (SEM) images of the film formed using phase inversion (left) and the PI-ST method (right) are shown in Figure 2a. Notably, the TPU film and interconnected porous structure are created simultaneously. NaCl particles are readily soluble in the Ag NW aq. solution, which is the nonsolvent in phase inversion. Thus, a conductive TPU film with a controllable interconnected porous structure is created using the PI-ST method. This structure acts as a sensitive layer of the touch sensor and is highly effective in improving the compressibility of TPU to significantly increase the sensitivity of the touch sensor.

Films based on various material systems are prepared using phase inversion to verify the generalizability of this technique (Figures S1 and S2, Supporting Information). The interaction parameters and apparent diffusivities of these ternary material systems are listed in Tables S1 and S2 in the Supporting Information.[15] Optical photographs of the TPU, polyvinylidene fluoride, polyacrylonitrile, cellulose acetate, polyvinyl chloride, and polystyrene micropore films and their corresponding cross-sectional SEM images are shown in Figure S2 in the Supporting Information. These images demonstrate the feasibility of this method for preparing touch sensors with different polymers. Additionally, the phase inversion processes of these polymers are shown in Movies S1 and S2 in the Supporting Information.

2.2. Interface Characteristics and Performance Optimization of the Sensitive Layer

The electromechanical properties of sensitive layers are crucial for ultrasensitive touch sensors. The content of Ag NWs is an important factor that affects the electrical properties of the sensitive layer.[17] The effective injection amount of Ag NWs in TPU can be increased through the mechanical mixing of these materials as composite polymers and the introduction of the Ag NW aq. solution as a nonsolvent. According to the formula for the percolation threshold,[18] the electroosmotic phenomenon occurs when the volume percentage of Ag NWs in TPU is 0.15 vol% (the corresponding mass fraction is 0.012 wt%). However, if the nonsolvent in-phase inversion is deionized (DI) water, the volume resistance is still high when the Ag NW content is considerably larger than the theoretical value. In contrast, the volume resistance of the composite film decreases by six orders of magnitude when the Ag NW aq. solution is used as the nonsolvent (Figure S3, Supporting Information). This proves that the Ag NW aq. solution increases the injection and entanglement of Ag NWs on the TPU skeleton with the interconnected porous structure during phase inversion. A light-emitting diode emits light even when the film is connected in series to the circuit; this demonstrates the excellent conductivity of the composite film (Figure S4, Supporting Information).

According to electroosmotic flow and tunnel conduction theory, the uniform distribution of conductive fillers (DMF solution of Ag NWs) in a polymer solution (DMF solution of TPU) affects the conductivity and response sensitivity of a prefabricated

© 2024 Wiley-VCH GmbH

15214095, 0, Downloaded from https://onlinelibrary.wiley.com/doi/10.1002/adma.202313857 by Cas-Beijing Institution Of, Wiley Online Library on [19/03/2024]. See the Terms and Conditions (https://onlinelibrary.wiley.com/terms-and-conditions) on Wiley Online Library for rules of use; OA articles are governed by the applicable Creative Commons License

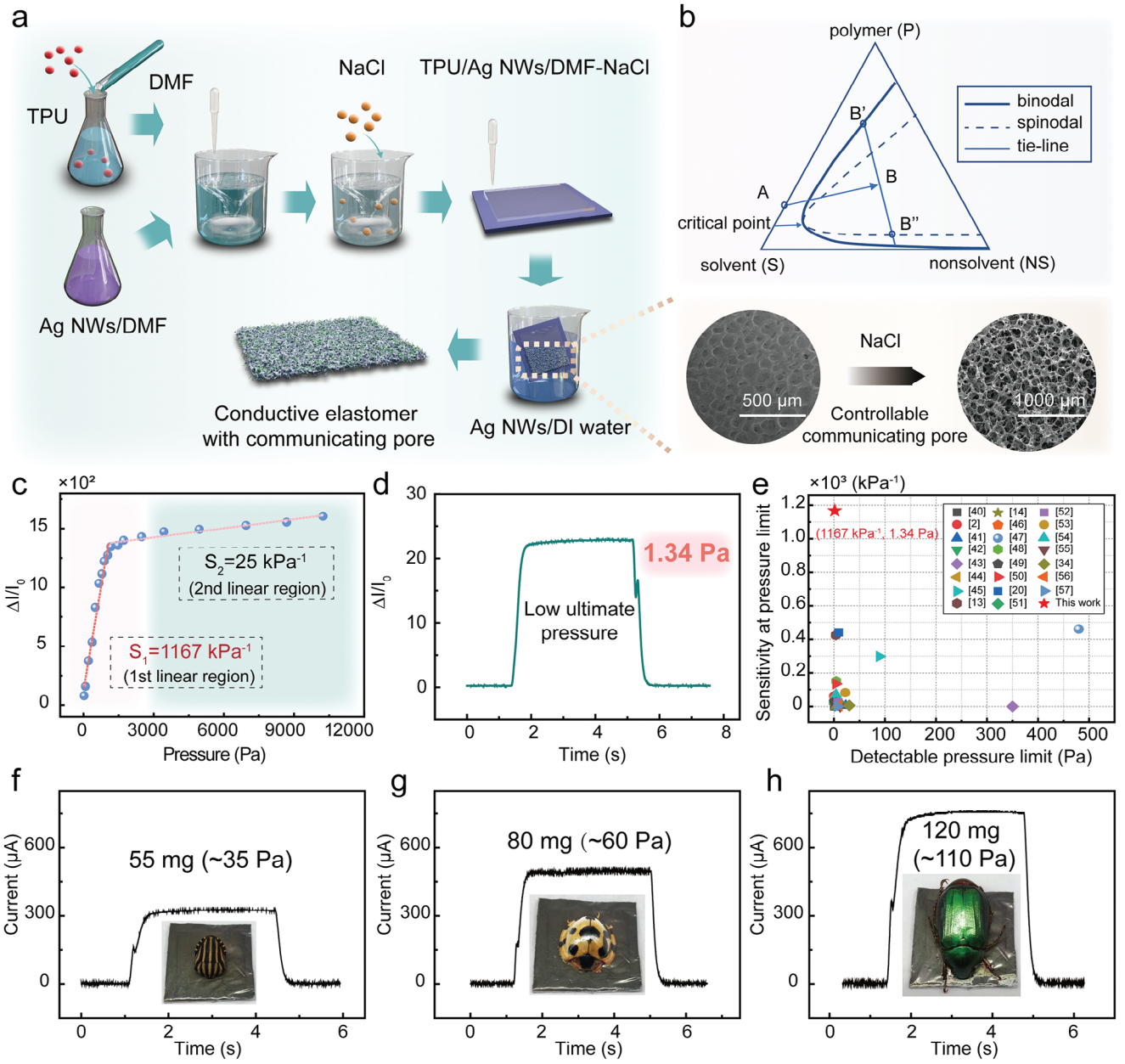

Figure 2. Technical route, principle, and performance of the touch sensor. a) Interconnected porous conductive films are prepared as sensitive layers for the touch sensors using the PI-ST method. The left inset shows the SEM image of the microporous film prepared using only phase inversion (scale bar: 500 μm). The right inset shows the SEM image of the interconnected porous film prepared using the PI-ST method (scale bar: 1000 μm). b) Film-formation mechanism of the phase inversion method. Thermodynamic analysis of the phase inversion method: a typical ternary phase diagram of liquid–liquid partition. c) Sensitivity and sensing range of devices with 45.4% porosity. d) Minimum detection limit of the device: 1.34 Pa. e) Comparison of the minimum detectable pressure and corresponding sensitivity at the pressure of the touch sensors with reported work. f–h) Monitoring of low static pressure by the sensor: insect specimens with different pressures.

composite film.[19] Thus, interface adhesion has been studied in the structure–activity relationship of touch sensors. Compared to the DMF solution of Ag NWs, the composite solution (DMF solution of Ag NWs and TPU) shows no significant sedimentation within 48 h, indicating better stability (Figure S5, Supporting Information). UV-visible spectroscopy is performed to further analyze the homogeneity of the composite solution (Figure S6, Supporting Information). The relationship between the Ag NW concentration and the absorbance of the composite solution at a wavelength of 409 nm (inset of Figure S6, Supporting Information) is approximately linear. This verifies the homogeneity of the composite solution.[20] A detailed analysis is provided in the Supporting Information. The energy spectrum of the composite films is obtained via energy-dispersive X-ray spectroscopy. The results show that C, N, O, and Ag are uniformly distributed in the analysis area (Figure S7, Supporting Information). Van der

© 2024 Wiley-VCH GmbH

15214095, 0, Downloaded from https://onlinelibrary.wiley.com/doi/10.1002/adma.202313857 by Cas-Beijing Institution Of, Wiley Online Library on [19/03/2024]. See the Terms and Conditions (https://onlinelibrary.wiley.com/terms-and-conditions) on Wiley Online Library for rules of use; OA articles are governed by the applicable Creative Commons License

Waals and frictional forces affect the stability of the interface between Ag NWs and TPU, resulting in the stability of the composite solution.[21] The results of Fourier transform infrared spectroscopy (Figure S8, Supporting Information), a wettability test (Figure S9, Supporting Information), and a friction theory test (Figure S10, Supporting Information) are presented in the Supporting Information.

The compressibility of the Ag NW/TPU composite film can be adjusted by varying the NaCl particle content to optimize the sensitivity of the device. All composite films with different porosities show uniform porous structures with pore sizes of 100–200 μm (Figure S11, Supporting Information). Tensile tests are carried out to investigate the mechanical properties (see the pressure–compressive strain relationship in Figure S12, Supporting Information). The composite film with a porosity of 45.4% exhibits the highest compressive strain under equal pressure, with an ultralow compressive modulus of 23.8 Pa (Figure S13, Supporting Information). An increase in porosity causes structural collapse owing to the insufficient supporting force of the composite skeleton. Deformation under compressive stress is investigated for the three samples under identical parameters (Figure S14, Supporting Information); the three curves overlap, indicating that the prepared films exhibit consistent mechanical properties.

2.3. Characterization of Pressure Sensing Properties

The aforementioned results verify that the compressibility of soft materials is significantly improved when an interconnected porous structure is introduced because air is more easily squeezed due to its low compressive modulus. Mathematically, the rate of variation in the interfacial contact area ($\Delta A/A_0$) increases with the porosity under compression. However, the initial contact area (A_0) is inversely proportional to porosity. Therefore, high porosity is conducive to the high sensitivity of touch sensors. It shows the electrical properties of sensors with different porosities, confirming that the sensitivities conform to the mechanical properties (Figure S15, Supporting Information). The degree of deformation of the composite film under different pressures helped to identify two regions where the touch sensor's sensing performance has a linear response to pressure. Figure S16 in the Supporting Information shows the SEM images of the composite film in different compressed states. The deformation becomes more limited as the compressive stress increases. The composite film with 45.5% porosity has a sensitivity of up to 1167 kPa^{-1} at pressures below 1179 Pa (Figure 2c), and the error bars for different samples with 45.5% porosity are provided in Figure S17 in the Supporting Information. The minimum pressure detection limit is as low as 1.34 Pa (Figure 2d), which is a significant improvement compared with that of conventional touch sensors (Figure 2e).[1b,6a,b,9,17,22] In addition, based on the comprehensive performance considerations of the sensors, we also conducted literature comparisons of other performance parameters, detailed information can be found in Figures S18–S20 in the Supporting Information. The sensitivity reaches 25 kPa^{-1} even in the sensing range of 1179–10 240 Pa. Touch sensors can perceive minor and weak stimuli in daily life owing to their high sensitivity. As shown in Figure 2f–h, insect specimens (weights in milligrams) are placed on the touch sensors with extremely low pressures of 35 Pa (55 mg), 60 Pa (80 mg), and 110 Pa (120 mg), respectively. Evident electrical output signals are generated even at these low pressures. This finding verifies that the proposed sensor provides a fast and stable response to low static pressures. Furthermore, a dynamic response can be achieved, as in the case of continuously falling water droplets and weak airflow (Figures S21 and S22, Supporting Information). This ultrahigh sensitivity makes the touch sensor suitable for the detection and discrimination of tactile and slip signals.

The current–voltage (I–V) curves of the touch sensor at different pressures are shown in Figure S23 in the Supporting Information. Ohmic contact is confirmed, and the resistance decreases as the pressure increases. The dynamic response curve shows that the sensor can provide a stable real-time response to a preset pressure gradient of 2–1000 Pa (Figure S24, Supporting Information). The response time of loading and the recovery time of releasing are 46.5 and 248.8 ms, respectively (Figure S25, Supporting Information). This apparent hysteresis may be caused by the viscoelasticity of the flexible TPU backbone. The repeatability and durability of the touch sensor are presented in Figure S26 in the Supporting Information. The sensor can sustainably function over 2000 loading and unloading cycles under a pressure of 500 Pa at 0.5 V.

2.4. Verification of the High Sensitivity of the Touch Sensor

The high sensitivity of the touch sensor is verified from other perspectives by attaching it to the carotid artery of an adult female experimenter (**Figure 3a**). The sensor can detect weak fluctuations in the carotid pulse and respiratory rate (Figure 3b). The pulse and respiratory rates are ≈84 beats min^{-1} and 12 cycles min^{-1}, respectively, which are consistent with the normal physiological indices of a healthy adult female in a calm state. Notably, the three characteristic peaks of the pulse, namely, P (percussion wave), T (tidal wave), and D (dicrotic wave), can be clearly observed (Figure 3c). In addition, the touch sensor can detect audio vibrations when it is placed on a phone while the phone is ringing. The Python programming language is used to extract the characteristic signals of the time domain for three different ringtones. Then, the frequency information is obtained using a short-time Fourier transform (Figure S27, Supporting Information). The signals collected by the touch sensor coincide with the specific characteristic peaks of the three ringtones in the time domain (Figure 3d–f). These weak signals can be monitored because of the high sensitivity of the sensor. This shows that the sensor can capture weak signals for slip sensing.

2.5. Signal Processing and Application of Slip Sensing

Another key advantage of a highly sensitive touch sensor is its ability to discriminate between tactile and slip sensing using a single sensor unit. After signals are collected by the touch sensor, an appropriate wavelet transform analysis method is used to extract the basic information for estimating whether slip occurs.[23]

Schematics of the experimental procedure, data acquisition, and signal processing are illustrated in **Figure 4a**, and the test apparatus is shown in Figure S28 in the Supporting Information.

© 2024 Wiley-VCH GmbH

15214095, 0, Downloaded from https://onlinelibrary.wiley.com/doi/10.1002/adma.202313857 by Cas-Beijing Institution Of, Wiley Online Library on [19/03/2024]. See the Terms and Conditions (https://onlinelibrary.wiley.com/terms-and-conditions) on Wiley Online Library for rules of use; OA articles are governed by the applicable Creative Commons License

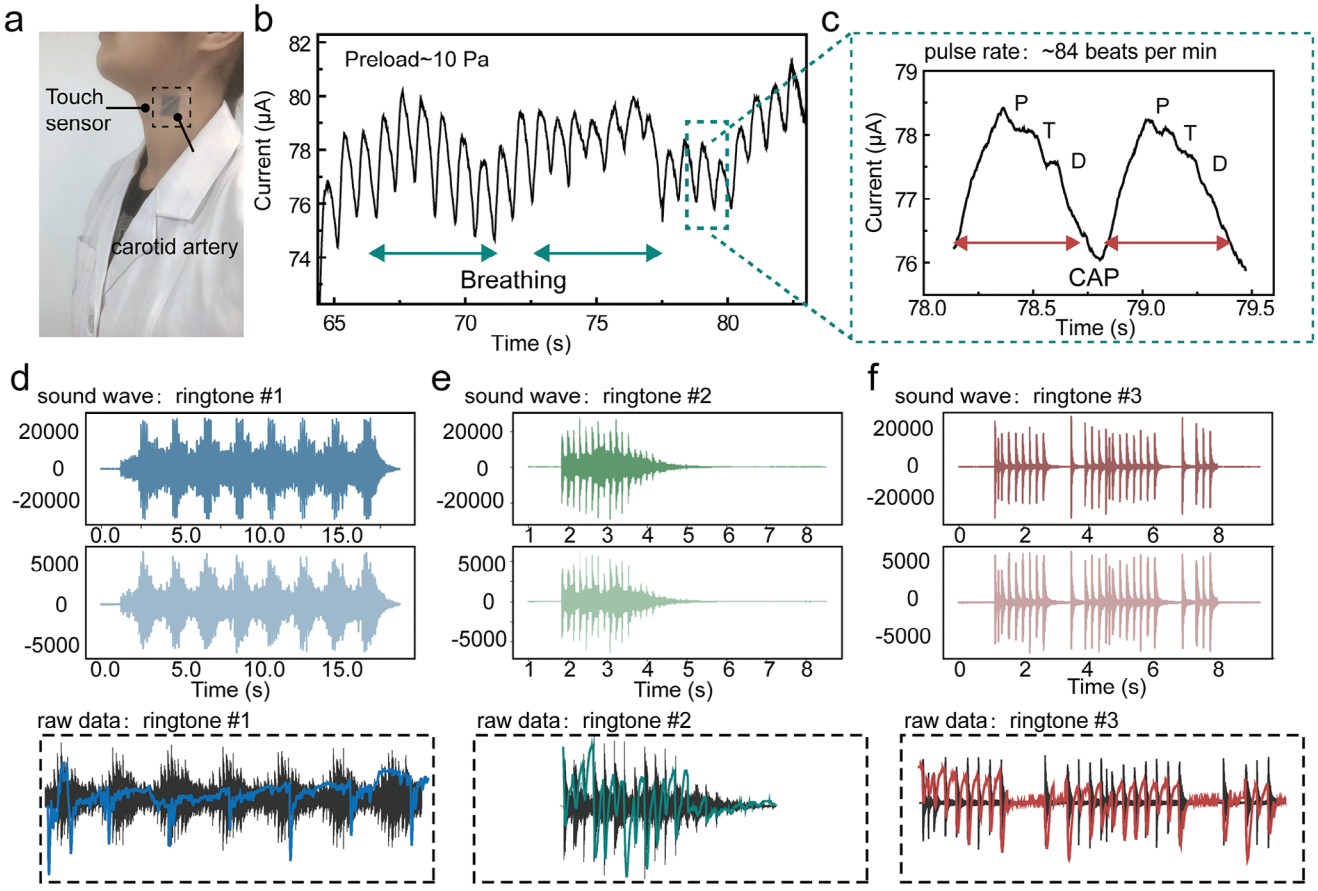

Figure 3. Verification of the high sensitivity of the touch sensor. a–c) Monitoring of weak physiological signals by the sensor. The sensor can detect weak fluctuations in the carotid pulse and respiratory rate. d–f) Monitoring of weak vibration signals by the sensor: three different ringing vibrations. The signals collected by the touch sensor coincide with the specific characteristic peaks of the three ringtones in the time domain.

The slipping process is simulated by pulling a weighted object on the surface of the touch sensor. The initial electric signal (current-time) and mechanical signal (tension-time) are collected and analyzed (Figure 4b). The variation in the tensile force is consistent with the change in current during a complete slipping process. The resistance of the sensor decreases due to an increase in the conductive path. Thus, the tension force (tangential deformation) applied on the sensor increases with the static friction force, resulting in a decrease in resistance and an increase in current (Figure S29, Supporting Information). Once slip occurs, the tensile force decreases slightly, accompanied by a slight decrease in current. At this moment, the interaction force between the sensor and object changes from static friction to kinetic friction.

In general, a stick–slip phenomenon occurs between the target object and the touch sensor. This phenomenon can affect the contact area, resulting in a fluctuation in the output signal.[9] As mentioned earlier, a weak signal can be captured by an ultrasensitive sensor when an object undergoes a slipping process. Continuous wavelet transform (CWT) and discrete wavelet transform (DWT) are applied to the current signal to magnify the signal difference between the slip and nonslip states. The specific analysis methods are shown in Figures S30 and S31 in the Supporting Information.[24]

The original electric curve, scale map, and intuitive time–frequency map are shown in Figure 4c. The slip process is broadly divided into four stages: i) In the first stage, the tangential deformation and the electrical output signal of the sensor remain unchanged in the presence of only the vertical normal force. Consequently, there are no high-frequency components at this stage. ii) In the second stage, the mutual tensile force and tangential deformation gradually increase. A high-frequency component is observed before the object begins to slip. iii) In the third stage, the tensile force continues to increase until it becomes equal to the maximum static friction force. At the moment of slipping, the tangential deformation of the sensor rapidly increases, leading to an increase in the conduction paths and corresponding high-frequency components. At this point, the highest frequency reaches ≈600 Hz. iv) The last stage shows the object in a slipping state. The tensile force is balanced by dynamic friction, and the number of conducting paths and the frequency of electrical signals are slightly larger than those in the first stage.

The signal generated by normal pressure is analyzed and compared with the slipping signal to exclude the interference of the frequency component caused by the change in the normal pressure during the slipping process (Figure 4d). Different frequency components are extracted from the signal by utilizing the DWT to process the electrical signal output. The maximum DWT detail

© 2024 Wiley-VCH GmbH

15214095, 0, Downloaded from https://onlinelibrary.wiley.com/doi/10.1002/adma.202313857 by Cas-Beijing Institution Of, Wiley Online Library on [19/03/2024]. See the Terms and Conditions (https://onlinelibrary.wiley.com/terms-and-conditions) on Wiley Online Library for rules of use; OA articles are governed by the applicable Creative Commons License

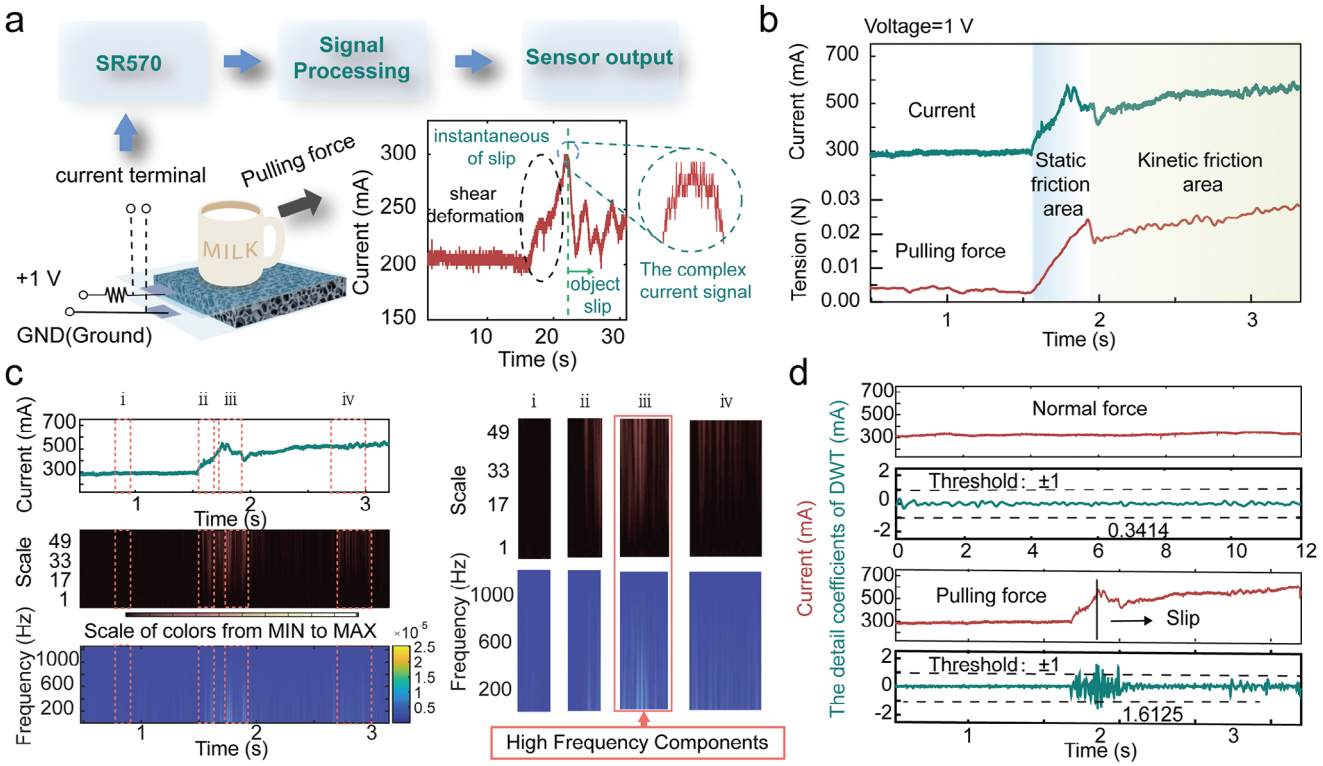

Figure 4. Principle and analysis method of slip sensing. a) Schematic of the acquisition system and analysis method. b) Curve of the tension and current applied to the object during a complete period from rest to slip. c) Local analysis of current signals generated by objects in different states through CWT and a time-frequency map. d) Curves of current transformation and results of DWT for objects subjected to normal pressure and tension force, respectively.

coefficient of the sensor is obtained under different force states. An appropriate slipping threshold is used to determine the occurrence of slipping on the basis of the results of the existing experimental analysis. Slipping occurs when the maximum DWT detail coefficient exceeds the slipping threshold. When normal pressure is applied to the sensor, the DWT detail coefficient shows a small overall fluctuation, with a maximum value of ≈0.3414. Under tension force, the DWT detail coefficient reaches its maximum value at the moment of slipping, with a value of ≈1.6125. In addition, on the basis of the surface roughness of the object, the slipping threshold of the object is assumed to be ±1 to carry out the subsequent experiments.

The slip signals of sandpapers with different values of surface roughness are measured using the touch sensor. The current output signal, DWT images, CWT images, and time–frequency graphs are shown in Figure S32 in the Supporting Information. The maximum DWT detail coefficient increases with roughness. This implies that as roughness increases, the vibrations caused by the change in the motion state become stronger, and it becomes easier to detect the slipping state.

Next, slip-sensing tests are conducted along the device surface using different weights (with acrylic at the bottom). The initial normal loads (weights) are set as 50, 100, 150, and 200 g. The slip speed of the weights is set to 5 mm s^{-1}. **Figure 5a** shows the raw signal of the current response during slipping. The DWT detail coefficients of the touch sensor with different mass loadings exceed the set threshold (±1) range before the instant when the object initially slips (Figure 5b). Moreover, the maximum DWT detail coefficient when slip occurs increases with the mass loading. This implies that the slip signal becomes stronger as the pressure increases. The corresponding CWT and time–frequency diagrams are consistent with the results shown in Figure 5c. This may be because the vibration of the sensor surface becomes stronger as the pressure increases. Therefore, slipping becomes easier to detect when the mass of the object increases.

Acrylic, cotton, and wood are selected as the contact surfaces between the weights and touch sensor, as shown in Figure 5d–g. The weights are 100 g each, and the slip speed is 5 mm s^{-1}. The DWT detail coefficient exceeds the set threshold (±1) range for all contact surfaces. The tensile force and maximum DWT detail coefficient are the smallest for the acrylic surface. This may be because acrylic is smoother than the other materials, leading to a small coefficient of friction and low sensor vibration. The static and sliding friction coefficients of the three materials are calculated according to the tensile force change curve recorded by a peel-force testing machine. The values are consistent with the analysis results, which verifies the potential of the ultrasensitive touch sensor for slip detection. To further validate the surface roughness of the materials, which involved in this experiment is analyzed by the 3D surface analyzer. Figure S33 in the Supporting Information shows a 2D profile of a wooden block and a 3D image of acrylic, respectively, as well as the surface roughness parameter, demonstrating the distribution of heights or depths within the sample area.

© 2024 Wiley-VCH GmbH

15214095, 0, Downloaded from https://onlinelibrary.wiley.com/doi/10.1002/adma.202313857 by Cas-Beijing Institution Of, Wiley Online Library on [19/03/2024]. See the Terms and Conditions (https://onlinelibrary.wiley.com/terms-and-conditions) on Wiley Online Library for rules of use; OA articles are governed by the applicable Creative Commons License

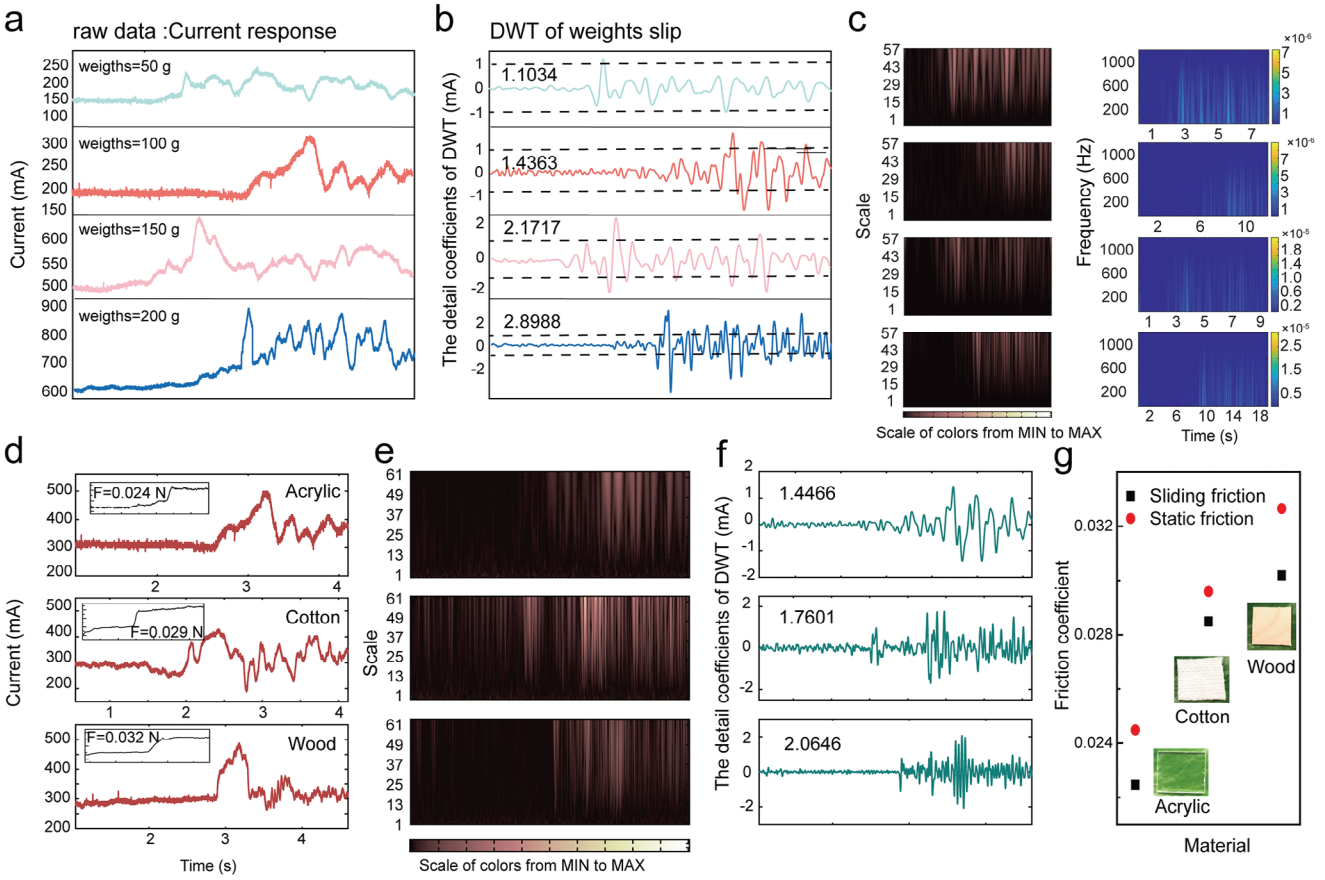

Figure 5. Influential factors and material identification in slip sensing. a–c) Analysis of slip signals of objects with different masses. Current output signal, DWT diagram, CWT diagram, and time-frequency diagram for objects with different masses when they slip relative to the device. d–f) Analysis of slip signals of objects with different materials. Tension and current variation curves, DWT diagrams, and CWT diagrams of objects with acrylic, cotton, and wood pasted on the bottom when they slip relative to the device. g) Static and sliding friction coefficients of acrylic, cotton, cloth, and wood obtained via calculation.

The sensor can distinguish between the contact forces for tactile and slip perception using a machine learning algorithm (Figure S34, Supporting Information). Data are collected for different contact forces and classified as tactile and slip forces. A total of 120 sets of data are tested for each contact force. The contact force dataset consists of 240 samples with a measurement length of 5 s per sample and a sampling rate of 500 Sps; the total number of data points is 5 × 500. We built machine learning models using two popular algorithms, namely, decision tree and multilayer perceptron. The confusion matrices of the two trained models show that the overall recognition accuracies for classifying tactile and slip forces are ≈98.75% and 100%, respectively. Such high accuracies are crucial for the automatic multimodal recognition required for intelligent sensing by manipulators.

3. Conclusion

High-pressure sensitivity is typically exhibited by touch sensors prepared from aerosol materials, while their detection range is quite narrow (below 1 Pa). In this article, we introduced a novel method to adjust the sensitivity layer structure and Young's modulus of pressure sensors, thereby achieving high-pressure sensitivity for elastic polymer materials over a wide detection range of ≈1 kPa. We developed a new sensing technology for complex contact states based on ultrahigh sensitivity pressure sensor components, which can be used to simultaneously detect positive pressure and slip states. A phase inversion method is introduced for the fabrication of flexible touch sensors. This method involves a short experimental period, minimal equipment requirements, and a low production cost. The method is demonstrated to be suitable for various material systems and can be used to improve the sensing performance of most elastic polymer materials used in the preparation of tactile sensors. Moreover, the combination of the phase inversion and sacrificial template methods overcomes the challenges in the formation of the interconnected porous structure in the polymer film. The sacrificial template is adjusted to modify the performance of the touch sensor and fabricate an ultrasensitive sensor. The sensor can successfully collect complex fluctuation signals and distinguish between tactile and slip forces by combining mathematical tools to extract signal features. This represents a new method for the fabrication of ultrasensitive touch sensors and provides a basis for investigating different contact force sensors.

© 2024 Wiley-VCH GmbH

15214095, 0, Downloaded from https://onlinelibrary.wiley.com/doi/10.1002/adma.202313857 by Cas-Beijing Institution Of, Wiley Online Library on [19/03/2024]. See the Terms and Conditions (https://onlinelibrary.wiley.com/terms-and-conditions) on Wiley Online Library for rules of use; OA articles are governed by the applicable Creative Commons License

4. Experimental Section

Preparation of Conductive Composite Films with Interconnected Porous Structures: An appropriate amount of TPU particles was added to DMF. The mixture was magnetically stirred at 60 °C for 6 h to form a homogenous solution with a mass fraction of 15 wt%. The Ag NW-DMF solution was diluted with DMF to achieve a suitable concentration. Then, the particles were uniformly dispersed using a magnetic stirrer. The diluted Ag NW-DMF solutions were added to TPU dropwise, and the process was carried out under continuous stirring at a speed of 800 rpm. Water-soluble NaCl particles with different masses were added to the Ag NW-TPU solution, and the mixture was continuously stirred until the particles were uniformly dispersed in the solution. Thus, a NaCl-Ag NW-TPU solution was obtained using DMF as the solvent. This solution was placed on a glass plate (8 × 4 × 0.2 cm in size) in a dropwise manner to allow it to flow naturally until a smooth and uniform liquid film was formed. Then, the liquid film was horizontally immersed in the Ag NW aq. solution for phase inversion until diffusion equilibrium was reached. The glass sheet was removed, and the formed solid film was peeled off and transferred to the Ag NW aq. solution for 30 min. Then, residual DMF and NaCl particles were removed via sonication. The amount of Ag NWs added to TPU was increased to obtain a conductive TPU film with a porous structure.

Preparation of Electrodes and Encapsulation Layers: A Ag/TPU nanofiber (NF) composite film was selected as the electrode layer to match the mechanical properties of the sensitive layer. The specific process was as follows: TPU NFs were obtained using the gas spinning technique. First, 7.5 g of TPU particles were dissolved in 50 mL of a DMF solution and magnetically stirred at 20–25 °C for 12 h at a speed of 1500 rpm to obtain a uniform TPU precursor solution. Thereafter, the TPU precursor solution was drawn into a plastic syringe, and the liquid was ejected outward at a constant rate of 0.5 mL h^{-1} using a programmable syringe pump. The NFs were obtained and collected on a receiver plate with regular holes. Finally, they were gently peeled off from the receiving plate and placed in a vacuum-drying oven at 50 °C for 6 h to remove any residual solvent. The ambient temperature and humidity during the entire air spinning process were controlled at 25 ± 5 °C and 40 ± 5%, respectively. The obtained TPU NF films were Ag-plated using magnetron sputtering to create a conductive layer. The magnetron sputtering power was 80 W, the sputtering time was 15 min, and the thickness of the Ag film was ≈150 nm. A commercially purchased polyethylene terephthalate (PET) film was used as the encapsulation layer during the experiment to improve the wear resistance and stability of the device. However, the encapsulation layer can be further improved to enhance the biocompatibility of the device.

Device Integration: The device used bottom-up integration in the following order: packaging layer (PET film), electrode layer (Ag-TPU NF composite film), sensitive layer (Ag NW-TPU composite film), electrode layer (Ag-TPU NF composite film), and packaging layer (PET film).

Characterization and Measurements: The surface morphologies of the samples were determined using SEM (Nova NanoSEM 450 and SU1510 Hitachi). The elemental types and contents of the material microregion components were analyzed using an energy-dispersive spectrometer (Nova NanoSEM 450 and Raith/EDAX). The contact angles of the samples were determined using a contact-angle analyzer (XG-CAMB1). The structural characteristics of the composite films were determined using a Fourier transform infrared spectrometer (VERTEX80v, Bruker). The composition, structure, and substance interactions of the composites were measured using an ultraviolet and visible spectrophotometer (Shimadzu/UV3600). The resistance of the composite films was measured using a megger (ZC36). A stepping motor (LinMot E1100) was used to apply normal pressure to the devices, and a commercial force gauge was used to detect this pressure (Nano17 ATI). A peel strength testing machine was used to apply a shear force to the devices and perform tensile testing (YL-S70). A synthesized function generator (DS 345) provided voltage to the devices, and a low-noise current preamplifier (MODEL SR570) was used to detect the current variations. The 3D surface analyzer (Bruker Contour GT-K) was used to analyze the surface roughness of the materials.

Supporting Information

Supporting Information is available from the Wiley Online Library or from the author.

Acknowledgements

The authors thank the Natural Science Foundation of Beijing Municipality (L223006, 2222088, Z180011), the National Key R&D Program of China (2021YFB3200302, 2021YFB3200304), the National Natural Science Foundation of China (U20A20166, 52192610, 61805015, 52125205, 61804011), the Shenzhen Science and Technology Program (KQTD20170810105439418), and the Fundamental Research Funds for the Central Universities for their support.

Conflict of Interest

The authors declare no conflict of interest.

Data Availability Statement

The data that support the findings of this study are available from the corresponding author upon reasonable request.

Keywords

phase inversion, sacrificial template, slip sensor, touch sensor, ultrasensitive

Received: December 18, 2023
Revised: February 5, 2024
Published online:

[1] a) Y. Zhang, Q. Lu, J. He, Z. Huo, R. Zhou, X. Han, M. Jia, C. Pan, Z. L. Wang, J. Zhai, *Nat. Commun.* **2023**, *14*, 1252; b) G. Gou, X. Li, J. Jian, H. Tian, F. Wu, J. Ren, X. Geng, J. Xu, Y. Qiao, Z. Yan, G. Dun, C. W. Ahn, Y. Yang, T. Ren, *Sci. Adv.* **2022**, *8*, eabn2156.

[2] a) K. Wang, W. Xu, W. Zhang, X. Wang, X. Yang, J. Li, H. Zhang, J. Li, Z. Wang, *Nano Res. Energy* **2023**, *2*, e9120042; b) Y. Lu, X. Qu, W. Zhao, Y. Ren, W. Si, W. Wang, Q. Wang, W. Huang, X. Dong, *Research* **2020**, *2020*, 2038560; c) G. Ge, Y. Lu, X. Qu, W. Zhao, Y. Ren, W. Wang, Q. Wang, W. Huang, X. Dong, *ACS Nano* **2020**, *14*, 218.

[3] a) L. Shi, Z. Li, M. Chen, T. Zhu, L. Wu, *Adv. Mater.* **2023**, *35*, 2210091; b) G. Ge, W. Yuan, W. Zhao, Y. Lu, Y. Zhang, W. Wang, P. Chen, W. Huang, W. Si, X. Dong, *J. Mater. Chem. A.* **2019**, *7*, 5949; c) J. Ren, W. Zhang, Y. Wang, Y. Wang, J. Zhou, L. Dai, M. Xu, *InfoMat.* **2019**, *1*, 396.

[4] a) Y. Zhang, J. Yang, X. Hou, G. Li, L. Wang, N. Bai, M. Cai, L. Zhao, Y. Wang, J. Zhang, K. Chen, X. Wu, C. Yang, Y. Dai, Z. Zhang, C. Guo, *Nat. Commun.* **2022**, *13*, 1317; b) X. Cai, S. Wang, L. M. Peng, *Nano Res. Energy* **2023**, *2*, e9120058; c) J. Ma, Y. Zhang, Y. Liu, D. Han, J. Mao, J. Zhang, W. Zhao, H. Sun, *Sci. Bull.* **2022**, *67*, 501.

[5] C. M. Boutry, M. Negre, M. Jorda, O. Vardoulis, A. Chortos, O. Khatib, Z. Bao, *Sci Robot.* **2018**, *3*, eaau6914.

[6] a) X. Shi, Y. Zhu, X. Fan, H. A. Wu, P. Wu, X. Ji, Y. Chen, J. Liang, *Matter.* **2022**, *5*, 1547; b) P. Min, X. Li, P. Liu, J. Liu, X. Q. Jia, X. P. Li, Z. Z. Yu, *Adv. Funct. Mater.* **2021**, *31*, 2103703; c) H. Xu, J. Tao, Y. Liu, Y. Mo, R. Bao, C. Pan, *Small* **2022**, *18*, e2202477; d) J. Xu, X. Li, H. Chang, B. Zhao, X. Tan, Y. Yang, H. Tian, S. Zhang, T. L. Ren, *ACS Nano* **2022**, *16*, 6687; e) S. Ding, M. Wang, H. Yang, F. Hu, Z. Dai, M. Lei, Q. Zhou, D. Zhao, Y. Gao, J. Zhong, J. Luo, B. Zhou, *Nano Energy* **2022**, *102*, 107671.

© 2024 Wiley-VCH GmbH

15214095, 0, Downloaded from https://onlinelibrary.wiley.com/doi/10.1002/adma.202313857 by Cas-Beijing Institution Of, Wiley Online Library on [19/03/2024]. See the Terms and Conditions (https://onlinelibrary.wiley.com/terms-and-conditions) on Wiley Online Library for rules of use; OA articles are governed by the applicable Creative Commons License

[7] T. Jin, Z. Sun, L. Li, Q. Zhang, M. Zhu, Z. Zhang, G. Yuan, T. Chen, Y. Tian, X. Hou, C. Lee, *Nat. Commun.* **2020**, *11*, 5381.
[8] M. Zhang, X. Gao, C. Lu, D. Yao, L. Wu, D. Li, H. Fang, S. A., Y. Sun, *ACS Appl. Mater. Interfaces* **2021**, *13*, 55735.
[9] Y. Yue, N. Liu, W. Liu, M. Li, Y. Ma, C. Luo, S. Wang, J. Rao, X. Hu, J. Su, Z. Zhang, Q. Huang, Y. Gao, *Nano Energy* **2018**, *50*, 79.
[10] a) J. C. Arezzo, H. H. Schaumburg, P. S. Spencer, *Environ. Health Perspect.* **1982**, *44*, 23; b) H. Tompa, *Polymer Solutions*, Butterworths Scientific Publications, New York **1956**; c) S. J. Lederman, R. L. Klatzky, *Atten. Percept. Psychophys.* **2009**, *71*, 1439.
[11] W. Yang, H. Liu, C. Liu, C. Shen, *Sci. Bull.* **2022**, *67*, 569.
[12] a) J. Shen, Y. Guo, S. Zuo, F. Shi, J. Jiang, J. Chu, *Nanoscale* **2021**, *13*, 19155; b) Y. Li, D. Han, C. Jiang, E. Xie, W. Han, *Adv. Mater. Technol.* **2019**, *4*, 1800504; c) J. Li, Z. Yuan, X. Han, C. Wang, Z. Huo, Q. Lu, M. Xiong, X. Ma, W. Gao, C. Pan, *Small Sci.* **2022**, *2*, 2100083.
[13] a) K. Fujimoto, M. Minato, S. Miyamoto, T. Kaneko, H. Kikuchi, K. Sakai, M. Okada, Y. Ikada, *J. Appl. Biomater.* **1993**, *4*, 347; b) B. Stropnik, V. Kaiser, *Desalination* **2002**, *145*, 1.
[14] X. Shi, X. Fan, Y. Zhu, Y. Liu, P. Wu, R. Jiang, B. Wu, H. A. Wu, H. Zheng, J. Wang, X. Ji, Y. Chen, J. Liang, *Nat. Commun.* **2022**, *13*, 1119.
[15] a) M. Mikawa, N. Seki, S. Nagaoka, H. Kawakami, *J. Polym. Sci., Part B: Polym. Phys.* **2007**, *45*, 2739; b) J. A. Van't Hof, A. J. Reuvers, R. M. Boom, H. H. M. Rolevink, C. A. Smolders, *J. Membr. Sci.* **1992**, *70*, 17.
[16] M. T. Khorasani, S. Shorgashti, *J. Biomed. Mater. Res., Part B* **2006**, *76*, 41.
[17] Y. Liu, J. Tao, W. Yang, Y. Zhang, J. Li, H. Xie, R. Bao, W. Gao, C. Pan, *Small* **2022**, *18*, e2106906.
[18] T. Nagai, N. Aoki, Y. Ochiai, K. Hoshino, *ACS Appl. Mater. Interfaces.* **2011**, *3*, 2341.
[19] S. I. White, R. M. Mutiso, P. M. Vora, D. Jahnke, S. Hsu, J. M. Kikkawa, J. Li, J. E. Fischer, K. I. Winey, *Adv. Funct. Mater.* **2010**, *20*, 2709.
[20] Y. Sun, B. Gates, B. Mayers, Y. Xia, *Nano Lett.* **2002**, *2*, 165.
[21] a) L. H. Shao, X. Qu, T. Wang, Z. Cui, Y. Liu, Y. Zhu, *J. Mech. Phys. Solids* **2023**, *173*, 105218; b) H. Zheng, W. Zhang, B. Li, J. Zhu, C. Wang, G. Song, G. Wu, X. Yang, Y. Huang, L. Ma, *Composites, Part B* **2022**, *233*, 109639.
[22] a) Y. Wang, M. Chao, P. Wan, L. Zhang, *Nano Energy* **2020**, *70*, 104560; b) C. L. Choong, M. B. Shim, B. S. Lee, S. Jeon, D. S. Ko, T. H. Kang, J. Bae, S. H. Lee, K. E. Byun, J. Im, Y. J. Jeong, C. E. Park, J. J. Park, U. I. Chung, *Adv. Mater.* **2014**, *26*, 3451; c) G. Y. Bae, S. W. Pak, D. Kim, G. Lee, D. H. Kim, Y. Chung, K. Cho, *Adv. Mater.* **2016**, *28*, 5300; d) Y. Ma, N. Liu, L. Li, X. Hu, Z. Zou, J. Wang, S. Luo, Y. Gao, *Nat. Commun.* **2017**, *8*, 1207; e) Y. Guo, M. Zhong, Z. Fang, P. Wan, G. Yu, *Nano Lett.* **2019**, *19*, 1143; f) M. Chao, L. He, M. Gong, N. Li, X. Li, L. Peng, F. Shi, L. Zhang, P. Wan, *ACS Nano* **2021**, *15*, 9746; g) Y. Jung, J. Choi, W. Lee, J. S. Ko, I. Park, H. Cho, *Adv. Funct. Mater.* **2022**, *32*, 2201147; h) S. Wang, W. Deng, T. Yang, Y. Ao, H. Zhang, G. Tian, L. Deng, H. Huang, J. Huang, B. Lan, W. Yang, *Adv. Funct. Mater.* **2023**, *33*, 2214503; i) Y. Cheng, Y. Ma, L. Li, M. Zhu, Y. Yue, W. Liu, L. Wang, S. Jia, C. Li, T. Qi, J. Wang, Y. Gao, *ACS Nano* **2020**, *14*, 2145; j) Y. Ma, Y. Cheng, J. Wang, S. Fu, M. Zhou, Y. Yang, B. Li, X. Zhang, C. W. Nan, *InfoMat* **2022**, *4*, e12328; k) X. Li, Y. Fan, H. Li, J. Cao, Y. Xiao, Y. Wang, F. Liang, H. Wang, Y. Jiang, Z. L. Wang, G. Zhu, *ACS Nano* **2020**, *14*, 9605; l) Y. Ma, Y. Yue, H. Zhang, F. Cheng, W. Zhao, J. Rao, S. Luo, J. Wang, X. Jiang, Z. Liu, N. Liu, Y. Gao, *ACS Nano* **2018**, *12*, 3209; m) K. Wang, Z. Lou, L. Wang, L. Zhao, S. Zhao, D. Wang, W. Han, K. Jiang, G. Shen, *ACS Nano* **2019**, *13*, 9139; n) Y. Liu, H. Xu, M. Dong, R. Han, J. Tao, R. Bao, C. Pan, *Adv. Mater. Technol.* **2022**, *7*, 2200504; o) D. Lee, J. Kim, H. Kim, H. Heo, K. Park, Y. Lee, *Nanoscale* **2018**, *10*, 18812; p) C. M. Boutry, Y. Kaizawa, B. C. Schroeder, A. Chortos, A. Legrand, Z. Wang, J. Chang, P. Fox, Z. Bao, *Nat. Electron.* **2018**, *1*, 314; q) Z. Wang, X. Guan, H. Huang, H. Wang, W. Lin, Z. Peng, *Adv. Funct. Mater.* **2019**, *29*, 1807569; r) C. B. Huang, S. Witomska, A. Aliprandi, M. A. Stoeckel, M. Bonini, A. Ciesielski, P. Samorì, *Adv. Mater.* **2019**, *31*, 1804600.
[23] J. Meyer, P. Lukowicz, G. Troster, in 2006 10th IEEE International Symposium on Wearable Computers, IEEE, Piscataway, NJ **2006**, pp. 69–72.
[24] L. P. A. Arts, E. L. van den Broek, *Nat. Comput. Sci.* **2022**, *2*, 47.

© 2024 Wiley-VCH GmbH

15214095, 0, Downloaded from https://onlinelibrary.wiley.com/doi/10.1002/adma.202313857 by Cas-Beijing Institution Of, Wiley Online Library on [19/03/2024]. See the Terms and Conditions (https://onlinelibrary.wiley.com/terms-and-conditions) on Wiley Online Library for rules of use; OA articles are governed by the applicable Creative Commons License